Construction and simulation of fiber optic stress wave sensing system based on wavelet packet-lamb wave damage imaging

X.L. Li [1], F. Liu [1], Q.N. Hui [1]
[1] College of Science, 710065, Xi'an, China, Xi'an Shiyou University

Abstract

Nowadays, various materials are extensively utilized in various fields. These materials often cause invisible damage with the long-term service of machines. A health monitoring system for materials was presented to eliminate safety hazards as much as possible. This study proposed a fiber optic stress wave sensing system in view of Lamb wave damage imaging to address the limitations in the use of materials in some flaw detection systems. Meanwhile, Lamb waves with small propagation attenuation and long distance in the material were selected as the detection method. Then the fiber optic stress wave sensing system was used to carry out damage imaging. The imaging principle of wavelet packet decomposition was selected to avoid losing low-frequency information. The experiment demonstrated that compared to the original method in view of time correlation coefficient, the method used in this study improved the signal-to-noise ratio of damaged images by 1.0112 dB, higher accuracy, better imaging quality, and more pronounced output images. This research offers a theoretical foundation for the application of fiber optic stress wave sensing systems in the flaw detection, provides practical value for the practical application of Lamb waves, and has positive significance for the application of flaw detection in industry.

Keywords: Lamb wave, damage identification, fiber optic sensors, wavelet packet decomposition.

Citation: Li XL, Liu F, Hui QN. Construction and simulation of fiber optic stress wave sensing system based on wavelet packet-lamb wave damage imaging. Computer Optics 2025; 49 (1): 44-52. DOI: 10.18287/2412-6179-CO-1491.

Introduction

In recent years, with the development of industry, various tools with long service lives and harsh operating environments have emerged. If the manufacturing materials of the tools are damaged during long-term use, these materials will lead to serious harm to the whole system [1]. For materials, the formation of damage is often divided into two stages: micro-damage and macro-damage. Microscopic damage originates from external forces or structural damage to the material itself, which gradually develops into macroscopic damage over time. At this point, the material will undergo brittle fracture, causing serious consequences [2]. Therefore, a relevant monitoring system of material structures has extremely important research significance to detect damage in the early stages [3]. In today's non-destructive testing, commonly used technologies include penetration testing, eddy current testing, magnetic particle testing, etc., but they often have some limitations in their use [4]. For example, magnetic particle testing technology is susceptible to electromagnetic interference. Penetrant testing technology can easily cause damage to human health during use. Eddy current testing technology has strict requirements for testing materials [5]. Therefore, this study proposed the use of elastic waves (Lamb) in free boundary solid plates as a detection method, which considers the plane wave transmitted in the free plate for flaw detection. Lamb has an extensive range of applying with appropriate cost and relevant consumption. Therefore, this research proposed a fiber optic stress wave sensing system in view of Lamb Wave (LW) damage imaging, which used the Wavelet Packet Decomposition (WPD) damage probability imaging algorithm to further improve the identification accuracy. The effectiveness and practicability of the proposed damage imaging method were verified by further experiments. There are two innovations. First, WPD is used for improving the recognition accuracy. The second is to introduce damage indicators as the core of the algorithm through algorithmic principles to further optimize the flaw detection system. This study is divided into four parts. The first part is a summary of relevant research fields. The second part is to build and optimize the system proposed in this study. The third part is for validating the system. The fourth part is a summary of this study.

1. Related works

In actual industrial operating environments, materials need to be exposed to rain, high temperatures, or dusty environments for a long time, so they are prone to damage. Therefore, the Structural Health Monitoring (SHM) is proposed for detecting material damage in an early and timely manner. Silik et al. proposed a new framework to accurately extract damage-related information features in building structures by selecting appropriate wavelets. It had high accuracy and was very effective [6]. Amer and Kopsaftopoulos proposed a new active sensing framework in view of ultrasonic guided waves in the wave-based SHM system, which had higher monitoring sensitivity and robustness [7]. Mao et al. proposed an im-

proved Bayesian modal identification method to reduce the impact of uncertain factors on measurement results during the measuring, ensuring the robustness of the iterative process while improving computational efficiency [8]. Huang et al. summarized different demerits about relevant testing techniques and discussed their advantages and disadvantages, and development suggestions were proposed [9]. Qhobosheane proposed a glass fiber reinforced polymer carbon nano-intelligent composite material with piezoresistive properties, which enhanced sensitivity to damage development [10]. Chen et al. proposed a tomographic imaging method for SHM, which realized the monitoring of tank or pipeline wall thinning. This method had high detection accuracy and was expected to be applied in the petrochemical industry [11].

In today's non-destructive testing, the energy forms used for testing are very diverse. Compared to other testing methods, they either have strict requirements for testing materials or testing environments. Some testing methods may even cause damage to human health. LW has great advantages as a detection method. Ye et al. proposed a method for identifying electrode defects in transmission tower bases in view of single-sided multipoint excitation of ultrasonic LW to address the difficult monitoring of buried grounding line networks. This method achieved precise quantification of grounding electrode defects and greatly reduced detection errors [12]. Zhao et al. proposed a LW fatigue crack prediction method in view of particle filter. The equation of state and the observation equation of crack growth were established. This method had high prediction accuracy [13]. Mousavi et al. used a new semi-three-dimensional method for simulating the propagation process of LW through a clamped ultrasonic gas flow meter in contact mode, which had better accuracy and lower energy consumption than traditional simulations [14]. Fakih et al. established a method to monitor the health status of different interfaces. An SHM system in view of LW and combined with artificial neural network was proposed, which accurately predicted the damage [15]. Abbasi and Honarvar investigated the frequency thickness's influence on the LW in special condition and confirmed the contribution changes of the LW modes observed in wave clusters [16]. Wu et al. proposed a damage shape recognition algorithm. This algorithm studied the rate of convergence of the method for grid size and time step, and its recognition results for damage at any position and irregular damage shape were more accurate [17]. Aiming at the performance optimization, Karpeev V et al. improved the periodic microstructure of the fiber optic sensor from the perspective of diffraction. The experimental results proved that it could effectively improve the transmission performance of the fiber optic sensor [18]. Karpeev V et al. proposed a strategy based on horizontal mode selection technology to enhance the sensing accuracy of fiber optic sensors, and the experimental results proved the excellent accuracy of this method [19]. Aiming at the mode coupling problem of multi-mode graded index fiber, Garitchev V et al. proposed to use computer-generated spatial filter to explore the coupling mechanism caused by periodic microbending. This method accurately analyzed the mode coupling phenomenon [20]. Karpeev V et al. further optimized the architecture of the fiber optic sensor on the basis of horizontal mode selection technology to further improve the performance of. The experimental results proved that this method effectively optimized the sensing performance [21].

Therefore, combining the above contents, it is very necessary to implement the current SHM system. It can ensure the detection and feedback of invisible damage in the material structure as soon as material damage occurs. Meanwhile, corresponding measures can be made in view of the damage situation to avoid major production accidents caused by material damage, thereby protecting property and personal safety. Therefore, this study further studies the SHM system. For improving the applicability of flaw detection, LW is selected as the detection means, and the fiber optic stress wave sensing system platform is built to implement flaw detection.

2. Construction of fiber optic stress wave sensing system platform in view of LW damage imaging

As the boost of industry, many tools or machines that operate in harsh environments have emerged. The materials of tools or machines are prone to damage due to long-term operation under extreme conditions such as rainwater, high temperatures, and even low temperatures. If the material damage is not detected in a timely manner, it will gradually deteriorate over time, ultimately leading to tool or machine damage, and even causing major production accidents, resulting in property and personal losses. Therefore, this study proposes a fiber optic stress wave sensing system in view of LW damage imaging. The LW is used to improve the applicability of the flaw detection system, the power consumption of the flaw detection system is reduced, a fiber optic stress wave sensing system is constructed, and the flaw detection system is optimized to improve its accuracy and practicality.

2.1. Construction of LW damage imaging system

LW is an essentially ultrasonic wave, as the speed, attenuation, and impedance of sound waves propagating in materials are relevant to the properties. Meanwhile, sound waves can scatter at material defects, thus detecting material damage [22]. The definition of LW is the stress wave obtained by coupling transverse and longitudinal waves in the waveguide when the thickness of the waveguide and the wavelength of the excitation wave are of the same order of magnitude. The LW that is symmetrical to the center of the plate and the surface vibration of the plate is called a symmetric LW, also called the S-wave. The LW with the same vibration direction on the upper and lower surfaces of the plate is called an anti-symmetric LW, also called the A-wave. Meanwhile, each type of wave will

undergo multiple modes in the plate due to dispersion phenomenon, so the symmetric LW is denoted as $S_0, S_1, S_2, \ldots, S_n$, and the antisymmetric LW is served as $A_0, A_1, A_2, \ldots, A_n$. The particle vibration of the two types of waves varies with the wave propagation process in the plate, as shown in Fig. 1.

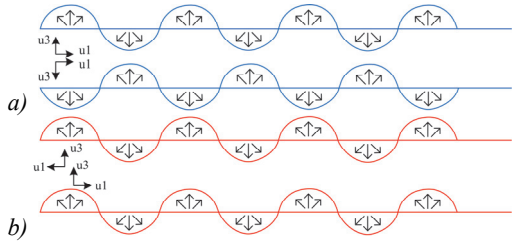

Fig. 1. Vibration of particles in a plate with different modes of waves. a) symmetric mode, antisymmetric mode

In each mode, the Group Velocity (GV)and Phase Velocity (PV) of the signal will change with the change of frequency. For better helping the application of LW flaw detection, it is essential for calculating the GV and PV of LW in different modes at different frequencies. Rayleigh Lamb formula [23] is used to describe the relevant characteristics of LW in two modes, as shown in Formula (1).

$$\begin{cases} \text{Symmetric mode} = \dfrac{\tan(qh)}{\tan(ph)} = -\dfrac{4k^2pq}{(q^2-k^2)^2} \\ \text{Asymmetric mode} = \dfrac{\tan(qh)}{\tan(ph)} = -\dfrac{(q^2-k^2)^2}{4k^2pq} \end{cases}. \quad (1)$$

Rayleigh Lamb formula describes the relation in PV and frequency thickness product in the process of LW propagation. This formula has infinite solutions, which means that LW possess multiple modes and exhibit dispersion during their propagation. It further explains the relevant parameters in Formula (1) and supplements it with Formula (2).

$$\begin{cases} p^2 = (\omega / c_l)^2 - k^2 \\ q^2 = (\omega / c_s) - k^2 \\ k = \omega / c_p \end{cases}. \quad (2)$$

In Formulas (1) and (2), h is half of the thickness of the propagating plate. c_l is the longitudinal Wave Velocity (WV) (constant) in the corresponding mode. c_s is the transverse WV (constant). $c_p$is the PV of LW. k is the number of LW. ω is the Angular frequency. Two of these constants are relevant to the numerical values of the transverse and longitudinal waves of LW and the material properties of the propagation medium. Formula (3) demonstrates the relevant calculation.

$$\begin{cases} c_s = \sqrt{G/\rho} \\ c_l = \sqrt{E/\rho} \end{cases}. \quad (3)$$

In Formula (3), E serves as the Shear modulus of the material. G represents the Young's modulus of elasticity of the material. ρ represents the density of the material. If the Shear modulus of the material is further expressed by the determined dimensionless quantity μ, and the Young's elastic modulus is expressed by the Dimensionless quantity quantity λ and μ as $E=\lambda+2\mu$, then the shear WV and the longitudinal WV can be further expressed. It is shown in Formula (4).

$$\begin{cases} c_s = \sqrt{G/\rho} = \sqrt{\mu/\rho} \\ c_l = \sqrt{E/\rho} = \sqrt{(\lambda+2\mu)/\rho} \end{cases}. \quad (4)$$

In Formula (4), the dimensionless quantities μ and v can be expressed by the Poisson's ratio v of the material, as shown in Formula (5).

$$\begin{cases} \mu = G = \dfrac{E}{2(1+v)} \\ \lambda = \dfrac{vE}{(1+v)(1-2v)} \end{cases}. \quad (5)$$

Rayleigh Lamb equation establishes the correlation between the PV of LW and the frequency thickness product. However, the GV of LW still needs to be solved, so it is assumed that a column of single frequency waves is Formula (6).

$$y_1 = \cos(\omega t - kx). \quad (6)$$

In Formula (5), the phase difference between two peaks of the same train wave is 2π, the distance difference is $L=2\pi/k$, and the time difference is $t=2\pi/\omega$. Thus, for a train of single frequency waves, its PV is as shown in Formula (7).

$$v = \frac{L}{t} = \frac{\omega}{k}. \quad (7)$$

The concept of GV can be explained by mixing two waves with the same amplitude but different frequencies. It assumes that the waves in two different columns are y_1 and y_2. Combined with the trigonometric identity transformation, the calculation method for the sum of the two columns of waves can be expressed as Formula (8).

$$y_1 + y_2 = 2A\cos(\bar{\omega}t - \bar{k}x)\cos(\Delta\omega t - \Delta k x). \quad (8)$$

In Formula (8), $\cos(\Delta\omega t - \Delta k x)$ represents the low-frequency carrier wave. $\Delta\omega$ represents the propagation frequency of the low-frequency carrier, and it can be concluded that the GV of the whole wave is $c_g=\Delta\omega/\Delta k$. $\cos(\bar{\omega}t - \bar{k}x)$ represents high-frequency wave. $\bar{\omega}$ represents the propagation frequency of high-frequency waves. It can be concluded that the PV of the whole wave is $c_p = \bar{\omega}/\bar{k}$. The GV of LW can be obtained through the calculation shown in Formula (9).

$$c_g = c_p^2[c_p - (fh)\frac{dc_p}{d(fh)}]^{-1}. \quad (9)$$

In Formula (9), c_g represents GV. c_p represents PV. $dc_p/d(fh)$ determines the relation coefficient in GV and PV. When $dc_p/d(fh)\to 0$, GV and PV are basically equal, so $c_g \approx c_p$. When $dc_p/d(fh)\to\infty$, $c_g \to 0$. By describing the relationship between PV and Angular frequency, the Dispersion Curve (DC) with frequency thickness product as independent variable and GV as dependent variable can be obtained. It is assumed that the experimental object is aluminum alloy 6061, with a transverse WV of 5303 m/s and a longitudinal WV of 2973 m/s. Fig. 2 indicates the details.

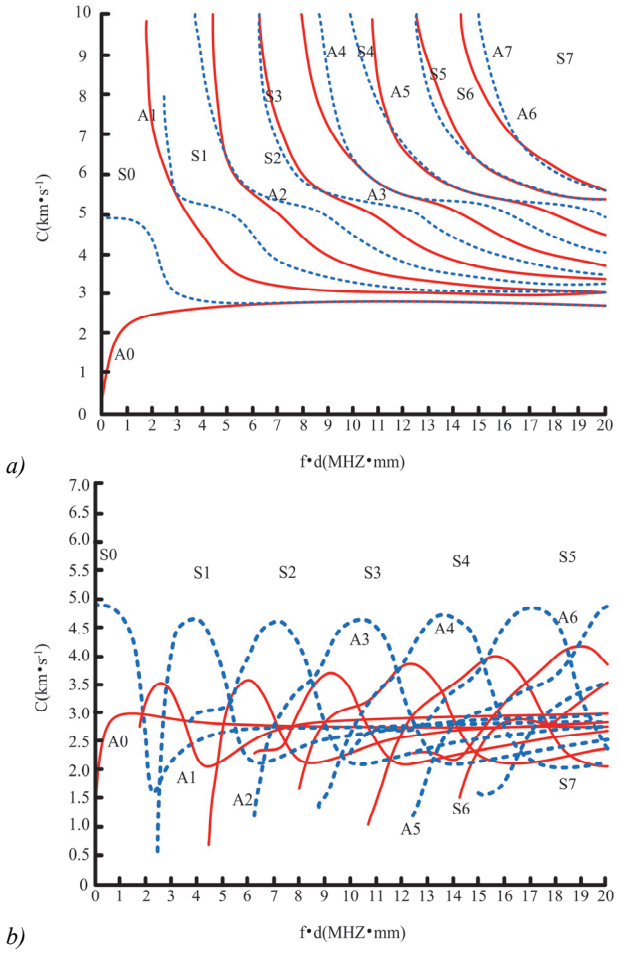

Fig. 2. DC of aluminum alloy 6061. a) Phase velocity dispersion curve of aluminum alloy 6061, b) group velocity dispersion curve of 6061 aluminum alloy

According to the scattering curve, the properties of LW can be obtained as follows: the frequency thickness product is nonlinear with GV and PV. For a flat plate with fixed material properties, there are more and more LW inside the plate as the frequency thickness product gradually grows. All other modes have cutoff frequencies, except for the S_0 and A_0 modes. When the frequency is less than the cutoff frequency, the modes will decay to dissipation. No matter how the frequency thickness product changes, there are always two or more modes. When the material properties change, the DC will vary depending on the solution of the Rayleigh Lamb equation, which in turn affects the cutoff frequency. In the health structure monitoring in view of LW, many damage indicators are extracted from signal features and compared with the signal indicators during health to determine the location and condition of damage. So the signals need to be processed before they are output, and Wavelet Transform (WT) is widely used as an emerging signal processing method in recent years. The change of the wavelet starts with the change of the basis of the transform. The Fourier basis is the basis of an infinite Trigonometric functions, while the WT is a finite length attenuated wavelet basis, which can obtain the frequency while positioning the time. The signal of LW can be positioned through the WT, as shown in Formula (10).

$$WT(a,b)=\frac{1}{\sqrt{a}}\int_{-\infty}^{+\infty} f(t)\Psi^*\left(\frac{t-b}{a}\right)dt\,. \tag{10}$$

In Formula (10), a represents the scale parameter of the WT. b represents the time parameter of WT. $f(t)$ is the signal representation of the original Lamb in the time domain. $\Psi(t)$ represents the wavelet basis function. $\Psi^*(t)$ represents the complex conjugate form of $\Psi(t)$. However, in Wavelet Decomposition (WD), signal decomposition often focuses on the low-frequency part, which makes the converted features often focus on the low-frequency part as well. This causes WD to lose more high-frequency features when facing nonlinear mechanical vibrations. Therefore, WPD is proposed on the basis of WD, and further decomposition is added. The whole decomposition process can be presented in the form of Binary tree, as shown in Fig. 3.

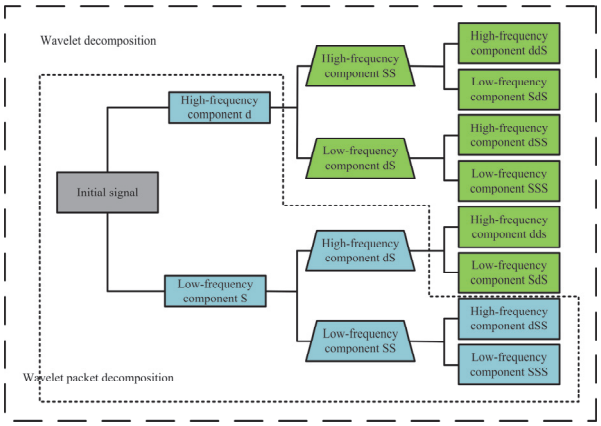

Fig. 3. Diagram of WD and WPD

2.2. Platform construction of fiber optic stress wave sensing system

The fiber optic F-P ultrasonic sensor is composed of two optical flat plates coated with reflective films on the inner surfaces. When a coherent beam of light enters the optical resonant cavity composed of the above-mentioned optical flat plates, multiple reflections occur, and a small amount of Transmitted Light (TL) is emitted during each reflection [24]. Therefore, further calculations can be made to obtain the reflectivity R_{FP} and refractive index (RI) T_{FP} of the F-P interferometer, as shown in Formula (11).

$$\begin{cases} R_{FP} = \dfrac{R_1 + R_2 + 2\sqrt{R_1 R_2}\cos\varphi}{1 + R_1 + R_2 + 2\sqrt{R_1 R_2}\cos\varphi} \\ T_{FP} = \dfrac{T_1 T_2}{1 + R_1 + R_2 + 2\sqrt{R_1 R_2}\cos\varphi} \end{cases}. \tag{11}$$

In Formula (11), T_1 represents the RI of the first lens. R_1 represents the reflectivity of the first lens. T_2 represents the RI of the second lens. R_2 represents the RI of the second lens. R_{FP} represents the ratio of FPI Reflected Light (RL) intensity to incident light intensity. T_{FP} represents the ratio of TL intensity to incident light intensity of FPI. The displacement generated by a round trip in an interferometer can be expressed as Formula (12).

$$\delta = \frac{4\pi n L}{\lambda}. \tag{12}$$

In Formula (12), n represents the RI of the medium in two mirrors. L represents the length of the cavity through which light passes. λ represents the wavelength of the incident light in vacuum. If the structure and position of the two mirrors are adjusted to maintain consistent reflectivity and RI, the normalized intensity of reflected and TL can be obtained as shown in Formula (13).

$$\begin{cases} I_r / I_0 = \dfrac{4R\sin^2(\delta/2)}{(1-R)^2 + 4R\sin^2(\delta/2)} \\ I_t / I_0 = \dfrac{(1-R)^2}{(1-R)^2 + 4R\sin^2(\delta/2)} \end{cases}. \tag{13}$$

By numerical simulations of the above equation, the normalized intensity curves of reflected and TL under different refractive indices R can be obtained, as shown in Fig. 4.

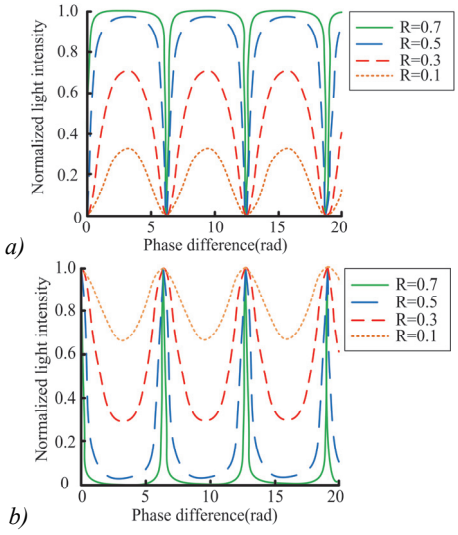

Fig. 4. Reflection and transmission normalized light intensity curves. a) normalized intensity of reflected light, b) normalized intensity of transmitted light

The simulation results indicate that there is a complementary relationship between the RL intensity and the TL intensity of multi-beam coherence. When $\delta = 2(m+1/2)\pi\,(m = 0, \pm1, \pm2, \ldots)$, the intensity of RL reaches the highest value and the intensity of TL reaches the lowest value. The intensity curve of RL changes with the RI R, and the larger the R value, the higher the slope of the curve near the minimum intensity of RL, while the curve near the maximum appears smoother. Further research is conducted on the light intensity of the F-P ultrasonic sensor. Air is used as the filling material inside the cavity. At this point, the reflectivity of the two mirrors is $R \approx 4\,\%$ or $(1-R) \approx 1$. At this point, the precision of the interferometer is no longer sufficient to measure its performance. The intensity of the reflected and TL is further simplified, and the simplified formula is obtained as shown in Formula (14).

$$\begin{cases} I_r = 2R(1-\cos\delta)I_0 \\ I_t = [1-2R(1-\cos\delta)]I_0 \end{cases}. \tag{14}$$

The light intensity formula indicates that when the power of the light source remains constant, the incident light intensity remains unchanged. Both the reflected and TL intensities have a correlation function between the sensor cavity length L variable and the phase shift δ of the light wavelength λ. When the wavelength of light remains fixed, external measured physical quantities can cause changes in the sensor cavity length L, changing the intensity of RL and TL. The change in cavity length L can also be inferred by the intensity variation characteristics of RL and TL, thereby achieving the detection of external physical quantities to be measured. The hardware of this experiment is mainly responsible for sensitive collection and form conversion of sensing signals. A high-speed four-channel fiber optic F-P cavity sensing signal conditioning system is used. The sensitivity of the thin film part of the probe is extremely high due to the high attenuation speed and large attenuation factor of LW in the flat plate. So the sensing membrane of Microelectromechanical Systems (MEMS) is selected in this experiment. The resonant center frequency of the processed film can be obtained in view of the deformation law of the film by using MEMS technology to process thin films, as shown in Formula (15).

$$f_c = \frac{\phi_{mn}^2}{4\pi r^2}\sqrt{\frac{E}{3\rho(1-\mu^2)}}. \tag{15}$$

In Formula (14), r represents the radius of the diaphragm. E serves as the Young's modulus of the sensing diaphragm material. ρ represents the density of the sensor diaphragm. μ represents the Poisson's ratio of the sensor diaphragm. The value of ϕ_{mn} is determined by the vibration mode of the diaphragm. Therefore, it indicates that the control of the resonant center frequency can be achieved by selecting the radius and material of the diaphragm. Therefore, the sensing membrane with a thickness of 400 μm, a cross-sectional edge length of 3 mm, a

suspended thickness of 10 μ*m*, and a suspended radius of 0.95 *mm* is calculated as the detection sensor membrane in view of the DC characteristics of LW and considering the preparation process. The structural schematic diagram of the sensor diaphragm and fiber optic LW sensing probe is shown in Fig. 5.

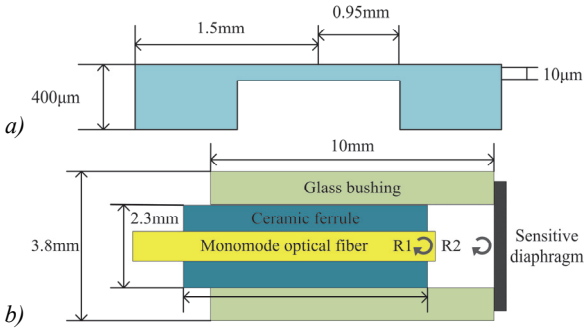

Fig. 5. Sensor film and probe schematic. a) sensor diaphragm diagram, b) sensor probe diagram

In this experiment, the Amplified Spontaneous Emission (ASE) light source is used. The operating wavelength range of ASE light source is 1527 *nm*–1562 *nm*, the spectral flatness is ≤3 *dB*, and the output light power is 23 *dBm*. The light with the central wavelength of 1550 *nm* is selected. According to the calculation in the previous article, when the central wavelength is 1550 *nm*, the three wavelengths required in the three wavelength demodulation are 1548.4 *nm*, 1550 *nm*, and 1551.6 *nm*. Then, the light with three central wavelengths is filtered out from the broadband light transmitted by the light source with the Dense Wave Division Multiplexing (DWDM) sensor. For the optoelectronic part, Field Programmable Gate Array (FPGA) is chosen to process the electrical signal. The FPGA used in this study selects the heterogeneous SOC ZYNQ7000 series launched by Xilinx in view of the system requirements, and XC7Z035-FFG676-2I (Kinex-7 architecture) is used to manipulate and control the timing, data, and transmission of each interface. The working voltage of the chip is 1.8*V*, and the maximum sampling rate is 65 *Mbps*. The hardware structure diagram is shown in Fig. 6.

3. Evaluation of fiber optic stress wave sensing system in view of LW damage imaging

In the practical engineering application, the SHM system needs to have certain recognition ability when facing these diversified environments. Therefore, this study verified the material damage situation in a LW-based fiber optic stress wave sensing system. The time-related damage imaging, the damage imaging in view of WD, and the damage imaging in view of WPD used in this study were chosen for experimental comparison to compare the experimental results. The selected experimental plate was an 800×800 *mm* – size aluminum alloy 6061 plate. The damage was set for the experiment. In the experiment, for ensuring the objectivity of the experimental outcomes, there were a large number of sensors arranged, as shown in Fig. 7.

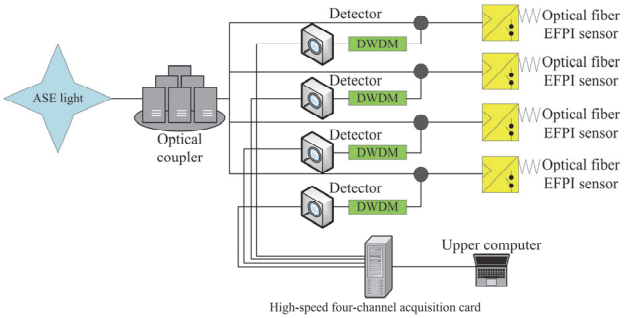

Fig. 6. Hardware structure of fiber optic demodulation instrument

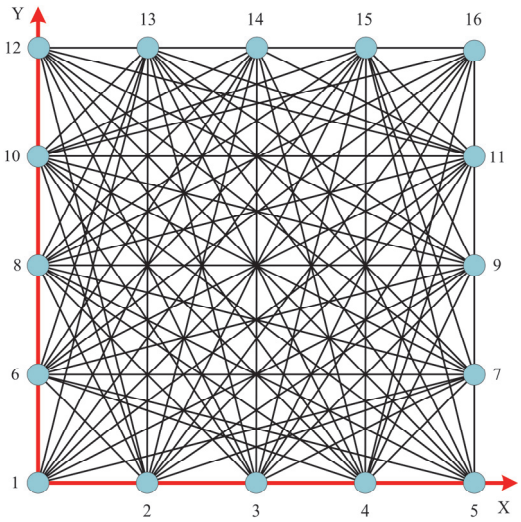

Fig. 7. Sensor full array sensor network diagram

In the arrangement of damage sensors within the entire flat plate, a circular through-hole damage with a radius of 20 *mm* was chosen. The reason for choosing this size and shape of the damage is that combining the size of plate 800×800 *mm* with the damage performance under the sensing network 300×300 *mm* can provide a clearer basis for analyzing the imaging effect of the algorithm. The damage settings on the sheet metal are shown in Fig. 8.

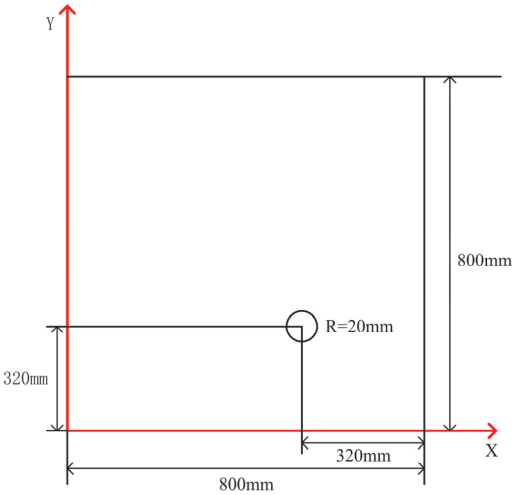

Fig. 8. Circular hole damage experimental design

Firstly, an initial damage probability algorithm in view of time correlation was chosen for experiments in

this study to verify the algorithm's performance after LW propagation on a flat plate. After the finite element simulation processing, the signals on the corresponding paths were sequentially exported to obtain the damage indicators on each sensing path. The damage index is the core of an algorithm, the larger the damage index, the greater the likelihood of damage remaining on that path. So this experiment obtained images comparing the size of damage indicators on each sensing path, as shown in Fig. 9.

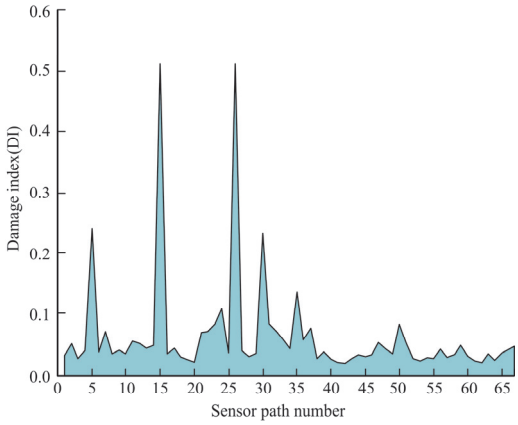

Fig. 9. Damage index in view of time correlation coefficient damage imaging

The amplitude of each pixel on the image was obtained after obtaining the damage indicators for each sensing path and processing them. The sensor array size in this experiment was 300×300 *mm*, so the imaging network of the entire image was divided into 300×300. After imaging processing, the damage imaging in view of time correlation coefficient was obtained, as shown in Fig. 10.

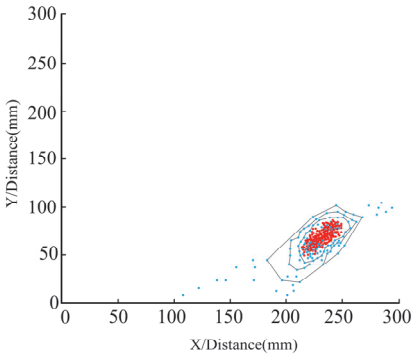

Fig. 10. Damage imaging in view of time correlation coefficient

In Fig. 10, the blue area represents the healthy part of the structure. The red area represents the damaged part. The curve around it is due to the propagation time of 0.005 s in the finite element simulation software simulation during simulation processing. This means that more echo resonance waves enter the algorithm's processing process, resulting in certain deviations in the imaging process. Applying the above imaging process scheme to the damage imaging in view of WD and WPD, the damage imaging can be obtained as shown in Fig. 11.

Although there were differences in their detection results through the analysis and comparison of the three structural damage maps, all three methods had dark red damage areas, which achieved localization of the damage location. So it is essential for further evaluating the quality of damage imaging among the three. The damage imaging signal-to-noise ratio and damage location judgment were used to evaluate the damage imaging results of the three methods, as shown in Tab. 1.

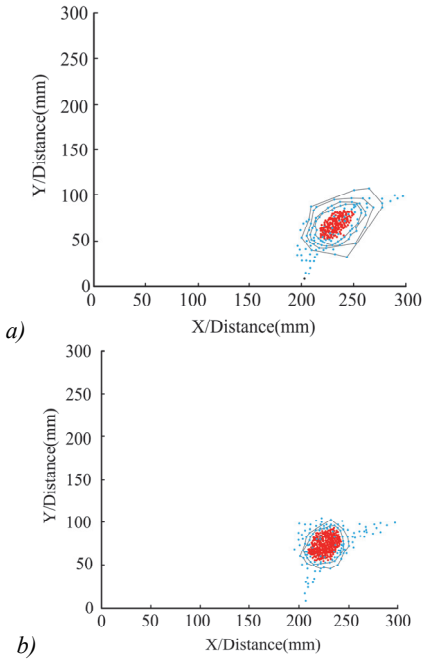

Fig. 11. Damage imaging in view of WD and WPD. a) damage imaging based on wavelet decomposition, b) damage imaging based on wavelet packet decomposition

Tab. 1. Comparison table of three damage indexes

Imaging principle	Based on time correlation coefficient	Based on wavelet decomposition	Based on wavelet packet decomposition
Determine damage location(mm)	(226, 82)	(232, 77)	(231, 78)
Relative error(mm)	(−4, 2)	(2, −3)	(1, −2)
Damage image signal-to-noise ratio	10.0012	9.3217	11.0124

In Tab. 1, the error between the damage shape in view of WPD and the real shape was the smallest in the damage location detection of the three damage indicators. Meanwhile, the error value in view of the time correlation coefficient was larger than that in view of the time correlation coefficient. Its shape was the most clustered at the damaged site. In terms of the signal-to-noise ratio of the damaged image, the signal-to-noise ratio in view of WPD was also the highest. This showed that the difference between the average strength of the damaged area and the healthy area was the largest in the damage monitoring image in view of WPD. That is to say, the damaged area in the image was more clearly displayed. This study continued exploring whether the damage probability imaging

algorithm in view of WPD still maintains good convergence in the experiment. The fitting curve results obtained after processing the experimental images are shown in Fig. 12.

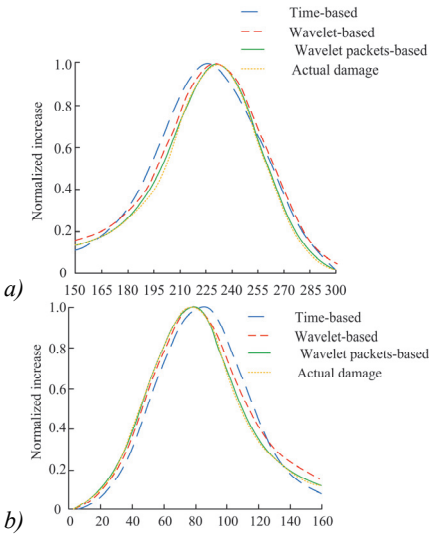

Fig. 12. Damage index amplitude comparison diagram. a) damage image horizontal coordinates, b) damage image ordinates

In Fig. 12, the damage imaging algorithm in view of WPD was basically consistent with the simulation, and the highest point of its curve was the closest to the actual damage coordinate. However, the time-based curve deviated relatively much, indicating that its positioning accuracy was still insufficient. In conclusion, the method in view of WPD adopted in this study had the highest accuracy, which indicated the effectiveness of the fiber stress wave sensing system in view of the LW damage imaging proposed in this study in the damage health monitoring. It effectively monitored material damage and had positive significance for the development of the industrial field.

Conclusion

In industrial applications, if structural damage to materials cannot be dealt with in a timely manner, it often leads to production accidents, property losses, and even threats to personal safety. Therefore, in this study, a damage probability imaging algorithm in view of fiber optic stress wave sensing system was proposed to emit LW from the material to be tested and evaluate the health of the material to be tested. On this basis, a damage assessment index in view of WPD was proposed to improve the damage probability algorithm to improve the effect of damage detection. In the experiment, a comparative experiment was conducted on damage imaging using methods in view of time correlation, WD, and the improvement of this research. The experimental results showed that, among the three methods, the damage imaging algorithm in view of WPD proposed in this study effectively extracted and characterized the difference between the characteristics of the health signal and the damage signal of materials. The damage image signal-to-noise ratio in view of WPD was increased by 1.0112 dB compared with the original method in view of time correlation coefficient, achieving better imaging effect. However, the material health monitoring system proposed in this study has high requirements for the placement of sensors in practical applications. If some sensors fail during the detection process, it will lead to significant errors in the results. When detecting different materials, the center frequency of the system needs to be recalculated in view of the DC of different materials, and its adaptability to different materials needs to be strengthened.

References

[1] Silva GFD, Souza EEPD, Filho EFDS, Farias PCMA, Albuquerque MCS, Sliva ICD, Farias CTT. Constrained neural classifier training method for flaw detection in industrial pipes using particle swarm optimisation. Int J Innov Comput Appl 2022; 13(3): 150-160. DOI: 10.1504/IJICA.2022.124239.

[2] Vivas G, Gabriel J, Etxaniz J, Aranguren G. Proof of concept for impact and flaw detection in airborne structures. Proced Struct Integr 2022; 37(1): 344-350. DOI: 10.1016/j.prostr.2022.01.094.

[3] Jiang S, Zhao L, Du C. Combining dynamic XFEM with machine learning for detection of multiple flaws. Int J Numer Method Eng 2021; 122(21): 6253-6282. DOI: 10.1002/nme.6791.

[4] Xu Q, Wang H, Chen Z, Huang Z, Hu R. Detection of cracks in aerospace turbine disks using an ultrasonic phased array C-scan device. Struct Durab Health Monit 2021; 15(1): 39-52. DOI: 10.32604/sdhm.2021.014815.

[5] Zhang M, Zhang W, Liang X, Zhao Y, Dai W. Detection of fatigue crack propagation through damage characteristic FWHM using FBG sensors. Sensor Rev 2020; 40(6): 665-673. DOI: 10.1108/SR-03-2020-0056.

[6] Silik A, Noori M, Altabey WA, Dang J, Ghiasi R, Wu Z. Optimum wavelet selection for nonparametric analysis toward structural health monitoring for processing big data from sensor network: A comparative study. Struct Health Monit 2022; 21(3): 803-825. DOI: 10.1177/147592172110102.

[7] Amer A, Kopsaftopoulos FP. Statistical guided-waves-based structural health monitoring via stochastic nonparametric time series models. Struct Health Monit 2022; 21(3): 1139-1166. DOI: 10.1177/14759217211024527.

[8] Mao J, Yang C, Wang H, Zhang Y, Lu H. Bayesian operational modal analysis with genetic optimization for structural health monitoring of the long-span bridge. Int J Struct Stab Dy 2022; 22(05): 2250051-2250074. DOI: 10.1142/S0219455422500511.

[9] Huang X, Wang P, Zhang S, Zhao X, Zhang Y. Structural health monitoring and material safety with multispectral technique: A review. J Safety Sci Res 2022; 3(1): 48-60. DOI: 10.1016/j.jnlssr.2021.09.004.

[10] Qhobosheane RG, Rabby MM, Vadlamudi V, Reifsnider K, Raihan R. Smart self-sensing piezoresistive composite materials for structural health monitoring. Ceramics 2022; 5(3): 253-268. DOI: 10.3390/ceramics5030020

[11] Chen M, Qiu H, Li F. SH guided wave tomography for structural health monitoring based on antiparallel thickness-shear (d_{15}) piezoelectric transducers. IEEE Sensors J 2021; 21(24): 27385-27392. DOI: 10.1109/JSEN.2021.3127005.

[12] Ye K, Zhou K, Zhigang R, Zhang R, Li C, Sun H, Huang S. Ultrasonic unilateral double-position excitation lamb

wave defect detection and quantification method for ground electrode of transmission tower. Int J Appl Electrom Mech 2022; 68(1): 29-43. DOI: 10.3233/JAE-210039.
[13] Zhao G, Liu C, Sun L, Yang N, Zhang L, Jiang M, Jia L, Sui Q. Aluminum alloy fatigue crack damage prediction based on lamb wave-systematic resampling particle filter method. Struct Durab Health Monit 2022; 16(1): 81-96. DOI: 10.32604/sdhm.2022.016905.
[14] Mousavi SF, Hashemabadi SH, Jamali J. New semi three-dimensional approach for simulation of Lamb wave clamp-on ultrasonic gas flowmeter. Sensor Rev 2020; 4(40): 465-476. DOI: 10.1108/SR-08-2019-0203.
[15] Fakih MA, Manuel C, Chiachío J, Mustapha S. A Bayesian approach for damage assessment in welded structures using Lamb-wave surrogate models and minimal sensing. NDT E Int 2022; 128(1): 102626-102648. DOI: 10.1016/j.ndteint.2022.102626.
[16] Abbasi Z, Honarvar F. Contribution of Lamb wave modes in the formation of higher order modes cluster (HOMC) guided waves. Proc Inst Mech Eng Pt C J Mechan Eng Sci 2022; 236(7): 3595-3605. DOI: 10.1177/095440622110424.
[17] Wu Y, Shen X, Li D. Numerical and experimental research on damage shape recognition of aluminum alloy plate based on Lamb wave. J Intell Mater Syst Struct 2021; 32(18-19): 2273-2288. DOI: 10.1177/1045389X21990885.
[18] Karpeev SV, Khonina SN. Optical fiber sensors based on diffractive and fiber periodic microstructures. In Book: Photonics elements for sensing and optical conversions. Ch 6. CRC Press, 2024: 158-177. DOI: 10.1201/9781003439165-6.
[19] Karpeev SV, Pavelyev VS, Khonina SN, Kazanskiy NL, Gavrilov AV, Eropolov VA. Fibre sensors based on transverse mode selection. J Mod Opt 2007; 54(6): 833-844. DOI: 10.1080/09500340601066125.
[20] Garitchev VP, Golub MA, Karpeev SV, Krivoshlykov SG, Petrov NI, Sissakian IN, Willsch R. Experimental investigation of mode coupling in a multimode graded-index fiber caused by periodic microbends using computer-generated spatial filters. Opt Commun 1985; 55(6): 403-405. DOI: 10.1016/0030-4018(85)90140-3.
[21] Karpeev SV, Pavelyev VS, Khonina SN, Kazanskiy NL. High-effective fiber sensors based on transversal mode selection. Proc SPIE 2005; 5854: 163-169. DOI: 10.1117/12.634603.
[22] Wang Z, Huang S, Wang S, Wang Q, Zhao W. Design of electromagnetic acoustic transducer for helical lamb wave with concentrated beam. IEEE Sensors J 2020; 20(12): 6305-6313. DOI: 10.1109/JSEN.2020.2976512.
[23] Maihulla AS, Yusuf I, Bala SI. Reliability and performance analysis of a series-parallel system using Gumbel-Hougaard family copula. J Comput Cogn Eng 2022; 1(2): 74-82. DOI: 10.47852/bonviewJCCE2022010101.
[24] Bai Y, Shen H, He Y, Wang L, Liu F, Geng X, Ren D, Liu S, Dang X, Li Y. Analysis of the stress-wave influence parameters of silicon MOSFET under 300V drain source voltage. IEEE Sensors J 2021; 21(18): 20107-20113. DOI: 10.1109/JSEN.2021.3094885.

Authors' information

Xiaoli Li, female, born in November 1981 in Fuxin City, Liaoning Province, is a Manchu ethnic group. She obtained a Bachelor's degree in Electronic Information Engineering in 2000 and a Master's degree in Optical Engineering in 2009. Her main research interests include fiber optic sensing and testing. Since 2004, I have been working at the College of Science at Xi'an Shiyou University. She has published three papers, authored two textbooks, invented two patents, and participated in two fund projects. E-mail: *xiaoli_li1981@163.com*

Fang Liu, female, born on December 16, 1977 in Tongchuan City, Shaanxi Province, of the Han nationality, obtained a Bachelor's degree in Computer Science Education in 2001 and a Master's degree in Computer Science and Technology in 2008. Her main research direction is computer software and theory. Since July 2001, she has been working at Xi'an Shiyou University. She has published two papers and participated in a funding project.
E-mail: *ring0163@126.com*

Qiannan Hui, female, born in September 1994 in Weinan, Shaanxi, of the Han nationality, obtained a Bachelor's degree in Optical Information Science and Technology in 2016 and a Master's degree in Optical Engineering in 2020. Her main research direction is digital holography. Since 2021, she has been working at the College of Science at Xi'an Shiyou University. E-mail: *tina09102023@163.com*

Received January 1, 2024. The final version – July 16, 2024.